Research Square

Preprints are preliminary reports that have not undergone peer review.
They should not be considered conclusive, used to inform clinical practice,
or referenced by the media as validated information.

Increased Moisture Amplifies Hazardous Humid-Heat in Africa's Great Green Wall

Cascade Tuholske

cascade.tuholske1@montana.edu

Department of Earth Sciences, Montana State University https://orcid.org/0000-0002-4806-0462

Catherine Ivanovich

NASA Goddard Institute for Space Studies

Emily Williams

Sierra Nevada Research Institute and Climatology Lab, University of California Merced

Radley Horton

Lamont Doherty Earth Observatory, Columbia University https://orcid.org/0000-0002-5574-9962

Shraddhanand Shukla

Climate Hazards Center, University of California, Santa Barbara

Chris Funk

University of California Santa Barbara

Kwaw Andam

International Food Policy Research Institute (IFPRI)

Christopher Kibler

Department of Geography, University of California, Santa Barbara

Edmund Yamba

Kwame Nkrumah University of Science and Technology

Andrew Zimmer

Oak Ridge National Laboratory

Nina Brooks

School for Environment and Sustainability, University of Michigan

Article

Keywords:

Posted Date: August 5th, 2026

DOI: https://doi.org/10.21203/rs.3.rs-10529227/v1

License: This work is licensed under a Creative Commons Attribution 4.0 International License.
Read Full License

Additional Declarations: There is **NO** Competing Interest.

Increased Moisture Amplifies Hazardous Humid-Heat in Africa's Great Green Wall

Authors: Cascade Tuholske[1,2,3,*], Catherine Ivanovich[4], Emily L. Williams[5], Radley M. Horton[6,7], Shraddhanand Shukla[8], Chris Funk[8], Kwaw Andam[9], Christopher L. Kibler[10], Edmund I. Yamba[11], Andrew Zimmer[2,3,12], Nina Brooks[13]

Affiliations:

[1]Aix Marseille Université, IRD, Inserm, SESSTIM, UMR1252, ISSPAM, Marseille, France
[2]Department of Earth Sciences, Montana State University, Bozeman, MT, USA
[3]Geospatial Core Facility, Montana State University, Bozeman, MT, USA
[4]NASA Goddard Institute for Space Studies, New York City, NY, USA
[5]Sierra Nevada Research Institute and Climatology Lab, University of California Merced, Merced, CA, USA
[6]Columbia Climate School, Columbia University, New York City, NY, USA
[7]Lamont Doherty Earth Observatory, Columbia University, Palisades, NY, USA
[8]Climate Hazards Center, University of California, Santa Barbara, Santa Barbara, CA
[9]International Food Policy Research Institute, Washington DC, USA
[10]Department of Geography, University of California, Santa Barbara, Santa Barbara, CA
[11]Department of Meteorology and Climate Science, Kwame Nkrumah University of Science and Technology, Kumasi, Ghana
[12]Geospatial Science and Human Security Division, Oak Ridge National Laboratory, Oak Ridge, TN, USA
[13]School for Environment and Sustainability, University of Michigan, Ann Arbor, MI, USA

[*]Corresponding author. Email: cascade.tuholske1@montana.edu

Abstract: The Great Green Wall aims to improve livelihoods and combat climate change across the Sahel. But interactions between greening and humid-heat have not been assessed. By harmonizing high-resolution climate data with vegetation and demographic datasets, we show that between 1983–2016 hazardous humid-heat days (HHD) in greening areas increased by 1.7-fold and 2.6-fold compared to areas with no vegetation change and decreasing vegetation, respectively. Amplified HHD intensity was more associated with elevated atmospheric moisture than air temperatures. In these areas, 45 million people (47% children) were exposed to >30 HHD in 2016. By 2050, nearly all Sahelian residents may experience >60 HHD per year. Our findings suggest that moisture may drive greening and elevate humid-heat risks, underscoring the need for adaptations that factor in humid-heat.

Main

The Sahel's 180 million residents face unprecedented risk from poverty, food insecurity, and climate change[1,2]. To address these challenges and support sustainable livelihoods, the Great Green Wall of the Sahara and Sahel Initiative (GGW) aims to restore 100 million hectares of degraded land by 2030[3]. While the efficacy and future of the GGW remain uncertain[4,5], vegetation growth may continue even without further anthropogenic land-cover and land-use change (LCLUC). Since the 1980s, the Sahel has greened due to increased precipitation[6–8], and climate change is projected to further green the Sahel in the coming decades[7].

In tandem with greening, hazardous humid-heat days (HHD) have rapidly increased[9,10] and are projected to increase further with climate change across the Sahel[9–12]. Exposure to HHD is already harming human health[13,14], food security[15], and economic productivity[16]. Rural residents – who are to benefit most from the GGW[3] – are especially vulnerable because their livelihoods depend on outdoor labor before and during the West African Monsoon (WAM)[17] when HHD peak[9,18]. While LCLUC-based adaptation like the GGW may decrease HHD risks (e.g., reducing air temperatures and providing shade), LCLUC can cause localized land-atmosphere feedbacks that can both attenuate and amplify atmospheric conditions that drive HHD (e.g., increasing humidity[11, 19]). This raises questions about the efficacy of greening as an adaptation to improve health and well-being in the Sahel.

We currently have little understanding of where LCLUC and changes in HHD are converging with demographic patterns across the Sahel. The few assessments of population exposure to HHD and future HHD projections for the region are coarse-grained[9,10,12], urban focused[20, 21], or imprecisely estimate the diurnal relationship between air temperature and atmospheric moisture during HHD [21, 22]. Therefore, it is unclear who faces increasing risk to HHD, how such risks relate to LCLUC, or how changes in the climatic drivers of HHD affect these events. This limits our ability to conduct cost-benefit analysis of LCLUC adaptations like the GGW[23].

Here, we map where LCLUC converges with changes in HHD and demographic patterns across the Sahel between 1983–2016 and we estimate future HHD exposure for 2050. To accomplish this, we merge high-resolution (5km) HHD estimates[24] with 5km short vegetation (SV)[25] and 1km age-stratified population data[26] (Materials and Methods). HHD are defined as a day in which the daily maximum heat index (HImax) exceeds 40.6°C, a threshold at which sun stroke and heat cramps are likely[9, 27].

We first examine the spatiotemporal evolution of HDD frequency and LCLUC across the Sahel between 1983–2016, measuring the total fitted change in the annual number of HHD for three SV categories: percent total decreased SV, no change in SV, and percent total increased SV (greening henceforth). Next, we measure whether HHD are intensifying or weakening because of changes in daily maximum air temperature (Tmax) or changes in atmospheric moisture – measured with relative humidity at the hour the daily maximum Tmax occurs (RHx) and daily average actual vapor pressure (AVPavg) – or both. Finally, to isolate future effects of climate change, we compare HHD exposure in 2016 with 5km HHD projections for 2050 under SSP2-4.5 ("middle of the road") scenario across historical SV categories, stratifying exposure by age cohort: children (0–15 years), working-age adults (16–64 years), and older adults (65+ years).

Results

Spatial and Temporal Co-Evolution of HHD and SV

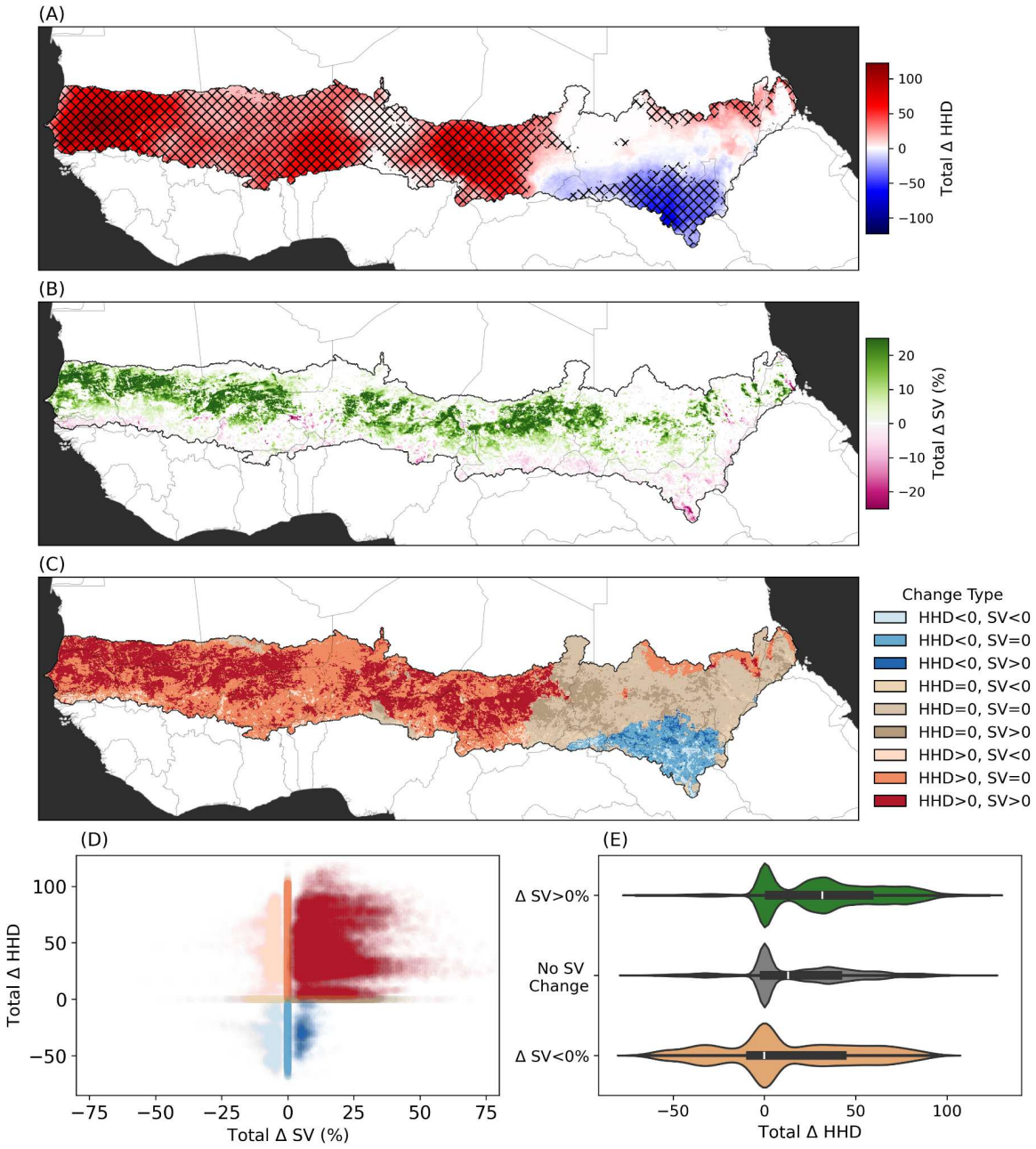


Fig. 1 Total Change in HHD Frequency and Short Vegetation

(A) Total fitted change in the annual number of hazardous heat days (HHD) from 1983–2016, estimated by multiplying the Theil-Sen slope (HHD yr^{-2}) by the 34-year study period. Hatched areas show statistically significant slopes ($p<0.05$; Kendall's tau test). HHD are days where HImax > 40.6°C. (B) Total percent change in short vegetation (SV) from 1982–2016. (C) Paired categories of total HHD change and total SV percent change during study period. (D) Pixel-level relationship between (A) and (B), correlating total HHD change with total SV change. (E) Distribution of total change in HHD binned by total SV change categories: SV>0% or total SV increase (green), no change (grey), and SV<0% or total SV decrease (tan). Kruskal-Wallis test and pairwise

MannWhitney U tests both show significantly different distributions among SV categories ($p<0.001$) in (E). Note that all non-statistically significant values in (A) are set to zero in (D) and (E).

On average, there were 23.9 more HHD in 2016 compared to 1983 across the Sahel. Total HHD increased across 62% (2.1 million km^2) of the region (Fig. 1A), spanning from eastern Chad to the Atlantic coast. SV increased by 5% on average. Greening covered 1.1 million km^2 (34%) concentrated in a northern, horizontal band (Fig. 1B). Greening hotspots include the Senegal River basin, the inland Niger River Delta, Lake Chad, and southeastern Sudan along the Nile River (Fig. 1B). No SV change and decreased SV covered 2 million km^2 (60%) and 200 thousand km^2 (6%), respectively.

Greening was highly spatially coupled with increased total HHD (Fig. 1C-E). On average, total HHD increased by 34 days in areas that greened, compared with 20 days in areas with no change in SV and 13 days in areas where SV decreased. That is, the increase in total HHD was 1.7 and 2.6 times higher in areas that greened compared to areas with no change in SV and SV decreased, respectively. Areas where SV and total HHD both increased span 26% (850 thousand km^2) of Sahel, an area where 54 million people (30%) lived in 2016. In areas that greened, 76% experienced an increase in total HHD (Fig. 1C-D). Areas of collocated greening and increased total HHD span the western Sahel, from Senegal to central Chad, with a gap along the western Niger border. Rapid increases in HHD (>60 total HHD) were concentrated in greening areas at low elevations (0–250 m) within the Senegal and Gambia River basins and at mid-elevations (250–500 m) near Lake Chad (Supplementary Fig. S1-S2), as well as low-elevations (0–250 m) with little greening along the Niger River south of Niamey.

East of Lake Chad, where weather patterns are less affected by the WAM and are more driven by sea surface temperatures in the Indian Ocean[28], strongly contrast the western Sahel. Areas with no HHD increase and no SV change are concentrated in the east (Fig. 1A-C), comprising 21% (690 thousand km^2) of the Sahel. Total HHD decreased along the Sudan-South-Sudan border (Fig. 1A), covering 8% of the Sahel (273,000 km^2). In these areas, total HHD decreased by 33 days in 2016 compared to 1983 on average. Notably, 57% of the area where total HHD decreased also experienced increases in total tree canopy (TC) (Supplementary Fig. S3A, Supplementary Fig. S4). However, the relationship between TC and decreased total HHD is not clear. Of the regions where TC increased – covering 13% of the Sahel – only 27% experienced a decrease in total HHD, whereas 36% experienced an increase in total HHD. Areas of both increased HHD and TC are concentrated in the southwestern Sahel along the Gambia River, Northern Ghana, and near Lake Chad.

The largest increases in total HHD per month occurred in the western Sahel during April - October, prior to and during the WAM (Fig. 2A). Areas west of central Nigeria faced a total increase of >=7 HHD during May. For June, this also included Lake Chad. By SV category, the long righthand tails in areas where SV increased during July–September indicate that the largest total HHD increase occurred during the WAM in greening areas (Fig. 2B). For example, between 2016 and 1983, in July the mean increase in total HHD in areas that greened was 1.6 times and 1.9 times of the increase in areas where SV did not change and SV decreased, respectively. The strongest decrease in HHD occurred during June, October, and November (Fig. 2A) along the Sudan-South-Sudan border. We note that during December - February HHD were rare across the Sahel (Supplementary Fig. S5-S7) and we find little observed changes in total HHD.

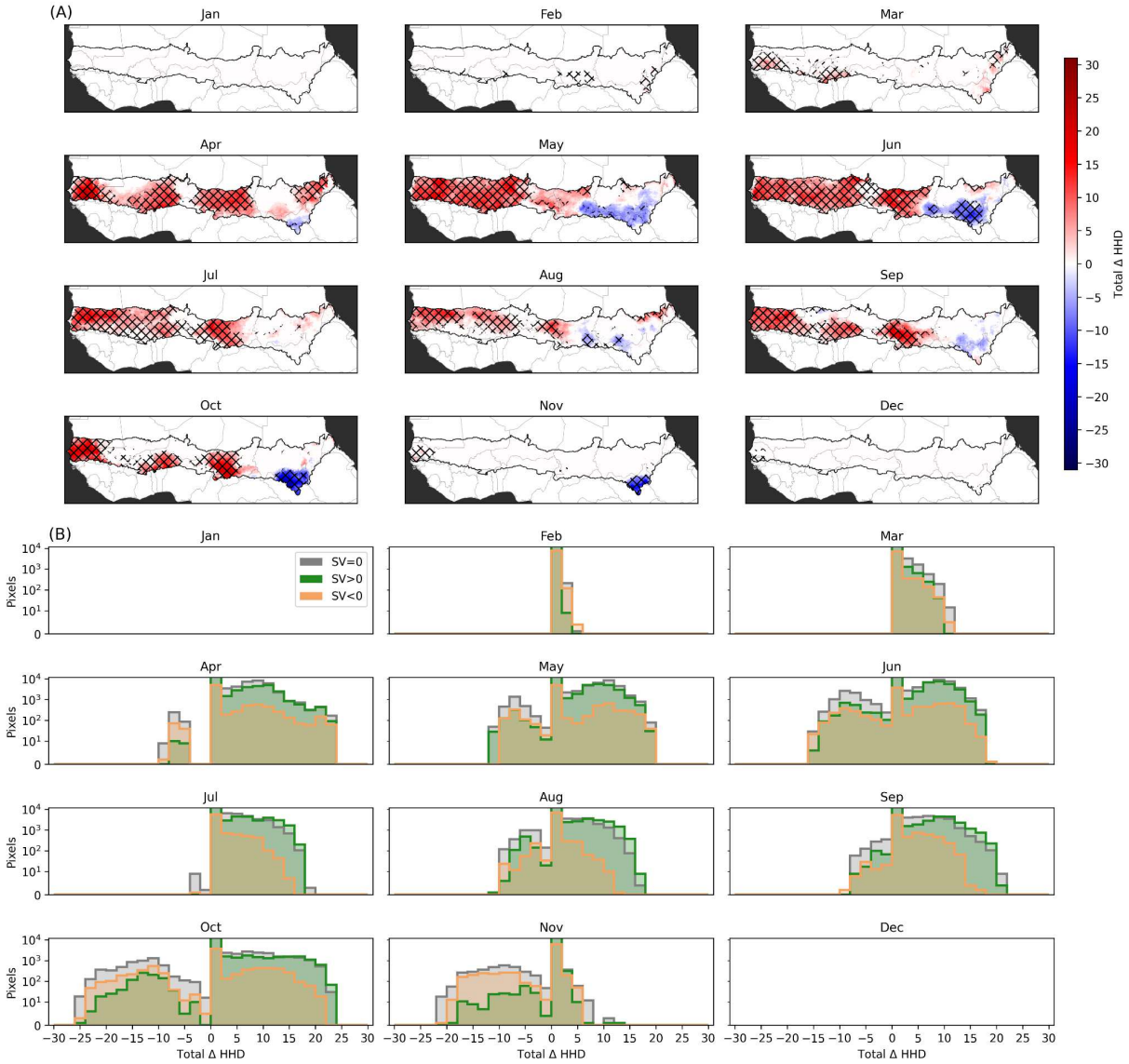


Fig. 2 Monthly Changes in HHD Frequency

(A) Total fitted change in number of hazardous heat days (HHD) per month from 1983–2016, estimated by multiplying the Theil-Sen annual trend (HHD per month) by the 34-year study period. Hatched areas show statistically significant slopes ($p<0.05$; Mann-Kendall test). HHD are days where HImax > 40.6°C. (B) Distributions of map area shown in (A) binned by total short vegetation change. Kruskal-Wallis test and pairwise MannWhitney U tests both show significantly different distributions among SV categories ($p<0.001$) for all months. Note all non-statistically significant values from (A) are set to zero in (B) and y-axes in (B) are displayed on a symmetric logarithmic scale to improve visualization.

Contributions to Increasing HHD Intensity

Similar to changes in HHD frequency (Fig. 1), we find that HHD intensity increased most rapidly in areas that greened (Fig. 3A, table S1). On average during a HHD in 2016, HImax was 0.32°C higher than in 1983 in areas that greened, compared with increases of 0.14°C and 0.03°C in areas

SV did not change or SV decreased, respectively (Fig. 3A). In contrast, we find that Tmax (Fig. 3B) during HHD increased least in areas that greened (0.03°C) and increased more substantially in areas where SV did not change (0.35°C) and SV decreased (0.38°C). AVPavg increased by 0.02 kPa in areas that greened but decreased by -0.07 kPa and -0.08 kPa in areas SV did not change and SV decreased, respectively (Fig. 3C). RHx exhibits a similar pattern (Fig. 3D). Together, this suggests that increasing HHD intensity in greening areas is primarily driven by rising atmospheric moisture rather than increasing air temperature.

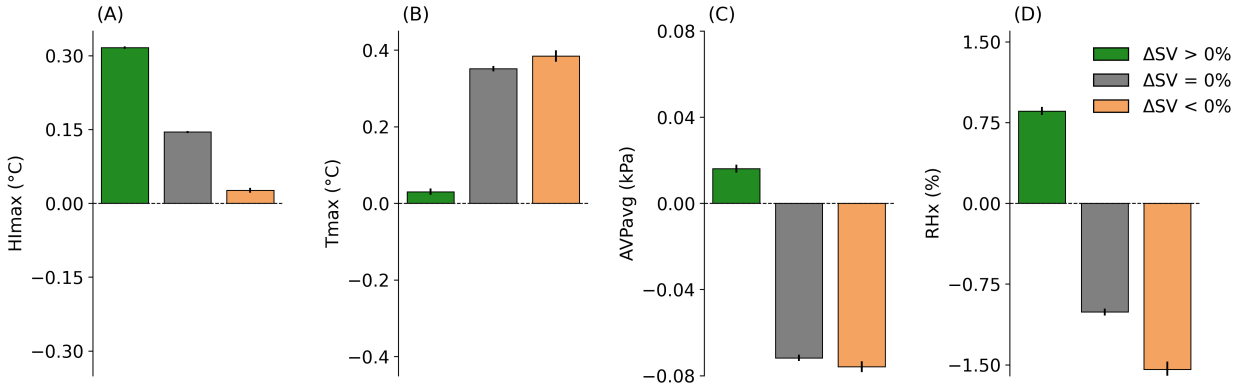


Fig. 3 Aggregated Change in HHD Conditions

Total fitted change in hazardous humid-heat day (HHD) conditions from 1983–2016 by short vegetation (SV) change category. Bars show the estimated total change in (A) HImax (e.g. HHD intensity), (B) Tmax, (C) AVPavg, and (D) RHx during a HHD in 2016 compared to 1983, calculated as the ordinary least squares (OLS) fitted trend multiplied by the number of HHD days in each SV category (Table S1). Colors indicate areas where SV increased (green), did not change (gray), or decreased (tan). Error bars represent ±1 standard error from OLS regressions with Newey–West heteroskedasticity- and autocorrelation-consistent (HAC) standard errors. All values are statistically significant ($p<0.05$; Mann-Kendall test).

Spatially, between 1983–2016, HHD intensity increased across the western Sahel and near Lake Chad (Fig. 4A), covering 43% of the entire Sahel. Tmax decreased during HHD along the Niger River and near Lake Chad (Fig. 4B), whereas atmospheric moisture increased in these regions (Fig. 4C-D). Along the Sudan-South-Sudan border, HHD intensity and atmospheric moisture decreased, but Tmax increased.

By SV category, HImax increased during HHD in 55% of the Sahel where SV increased, compared to only 38% and 30% in areas where SV did not change and decreased, respectively (Fig. 4E). Tmax increased during HHD for 16% of areas where SV increased, compared to 30% and 39% (Fig. 4F) in areas where SV did not change and decreased, respectively. Atmospheric moisture exhibited a contrasting pattern (Fig. 4G-H), as shown by the right-skewed distribution in areas where SV increased (Fig. 4G-H). For instance, AVPavg increased during HHD in 17% of areas where SV increased. But in areas where SV did not change or decreased, AVPavg increased in only 12% and 9% of areas, respectively.

The most widespread increase in HHD intensity occurred in May and June in the western Sahel and near Lake Chad (Supplementary Fig. S8A), just before the WAM. Increased Tmax was not widespread in the western Sahel across all months (Supplementary Fig. S9A) and we find pockets of decreasing Tmax in the western Sahel and around Lake Chad during August, during the WAM. Similarly, atmospheric moisture (Supplementary Fig. S10A and Supplementary Fig. S11A)

increased in much of the western Sahel during August and September. By SV category, the largest increases in HImax during HHD occurred in August and September in areas that greened (Supplementary Fig. S9B), during which the largest decreases in Tmax (Supplementary Fig. S10B) and largest increases in atmospheric moisture occurred in areas that greened (Supplementary Fig. S10B and S11B).

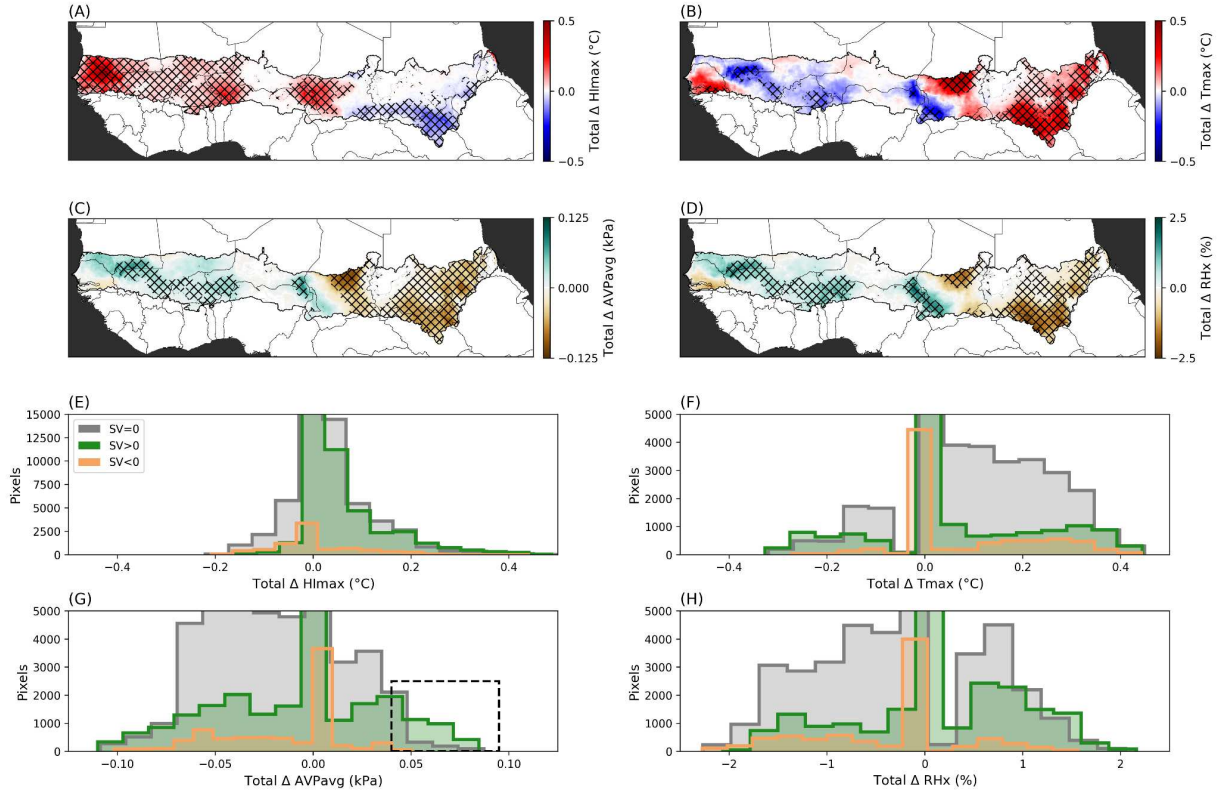


Fig. 4 Spatial Change in HHD Conditions

Spatial distribution of total fitted change in (A) HImax, (B) Tmax, (C) RHx, and (D) AVPavg during all HHD between 1983-2016 for the African Sahel. Hatching demarcates where fitted trends are significant at $p<0.05$ (Materials and Methods). Total fitted change in (E) HImax, (F) Tmax, (G) RHx, and (H) AVPavg binned by SV categories. Statistically insignificant ($p>0.05$) slopes shown in panels (A) – (D) are set to zero for the histograms in panels (E) – (H). Kruskal-Wallis test and pairwise MannWhitney U tests both show significantly different distributions among SV categories ($p<0.001$) for (E) – (H). Dashed box in (G) highlights long tail increases in AVPavg in areas that greened. Note that all non-statistically significant values from (A)-(D) are set to zero in (E)-(H).

Historical and Future HHD Exposure

In 2016, 122 million people (68%) were exposed to >30 HHD (Fig. 5A) in the Sahel. Some 45 million people lived in areas where SV increased. Nearly 80 million people (42%) were exposed to >60 HHD in 2016. Of these, 12 million were working-aged adults and 11 million were children who lived in areas that greened. Holding both population and total SV change constant in 2016, by 2050 nearly the entire Sahel – 166 million people – is projected to face >60 HHD under SSP2-4.5 "middle of the road" scenario (Fig. 5C). That is to say, 93% of children in 2016 are projected to face greater than 2 months of HHD by their peak working years. Similarly, 93% of working aged populations in 2016 are also projected to face greater than 2 months of HHD as they reach old age.

Along with densely-populated urban areas, hotspots of historical HHD exposure were concentrated in major river basins, including the Senegal, Gambia, Niger, Nile Rivers, as well as around Lake Chad (Fig. 5C). As noted previously, many of these are also greening hotspots. However, by 2050 (Fig. 5D), holding population and LCLUC change constant in 2016, regions of HDD exposure are projected to expand substantially with continued anthropogenic climate change. Future hotspots include much enlarged areas in northern Nigeria and Southern Niger, as well as Western Senegal, the Gambia, near Lake Chad, and eastern Sudan.

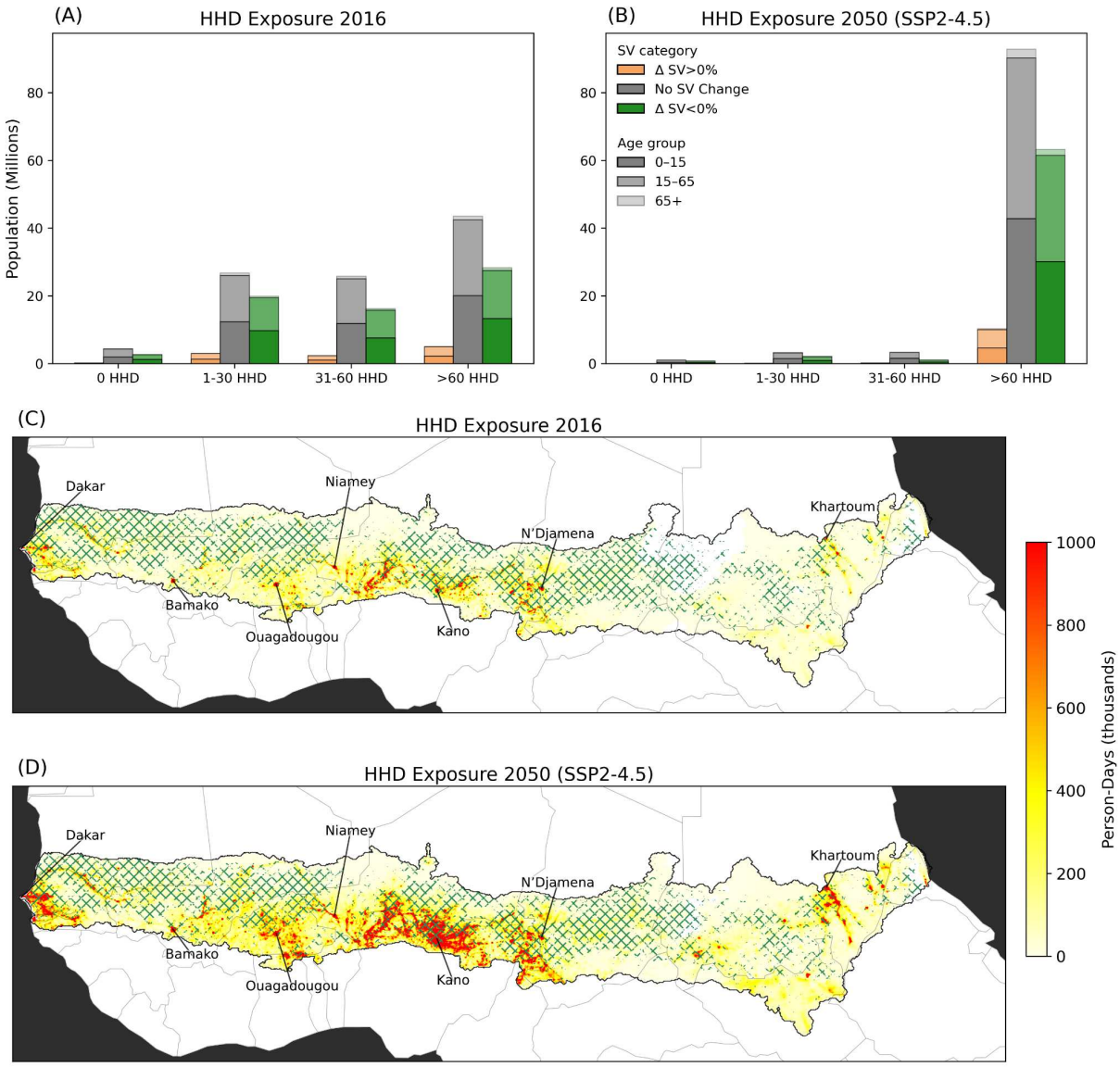


Fig. 5 Historical and Future HHD Exposure

Age-stratified population exposed to total HHD in 2016 (A) and 2050 following SSP2-4.5 (B) for the Sahel. Spatial distribution of HHD exposure (person-days) in 2016 (C) and 2050 following SSP2-4.5 (D). Green hatching shows the areas where total short vegetation (SV) increased during 1982-2016. Note that for all panels, both total SV change and population are held constant for 2016.

Discussion and Conclusion

Our results reveal a tight coupling of increased HHD frequency and increased greening across the Sahel. Conversely, in areas where SV did not increase, HHD frequency increases were less substantial. Changes in HHD intensity followed a similar pattern: In regions of increased SV, elevated atmospheric moisture – not increased air temperatures – tend to amplify HHD intensity. Changes in HHD intensity were more muted in areas that did not green, with increased Tmax playing a more important role in HHD intensity than atmospheric moisture. This suggests that elevated atmospheric moisture may be associated with both increased vegetation and HHD intensity (Fig. 3 and Fig. 4) in the Sahel, despite climate-change-driven increases in average air temperatures across the Sahel since the 1980s[29].

Though we do not assess the physical drivers of increased atmospheric moisture during HHD, there are several possible factors which may explain why elevated atmospheric moisture increased HHD intensity in greening areas. First, the WAM has intensified since the 1980s[30–32]. Modeling and observational analyses indicate precipitation increases are a dominant driver of Sahel greening [6–8]. We too find that atmospheric moisture (Supplementary Fig. S10-S11) and total rainfall (Supplementary Fig. S12) increased during July - September. Increased water vapor may also increase the trapping of longwave radiation, increasing the HHD intensity during May - June, prior to the WAM[18].

Second, as a response to increased precipitation, land-atmosphere coupling at localized scales can contribute to increased HHD intensity. Increased soil moisture spurs evapotranspiration, leading to greater local atmospheric moisture (and often decreased air temperatures), thus amplifying humid-heat anomalies in the Sahel[33–35]. This pathway suggests that humid-heat may be further amplified by local surface greening relative to nearby areas that have not greened. Third, local sea-surface temperatures can also influence HHD[36], which may be an important factor explaining the increase in HHD intensity near the Atlantic and Red Sea coasts. Together, our results motivate further regional climate modeling and in-situ data collection to explicitly evaluate the physical drivers of increased HHD frequency and intensity.

Given that regional climate models suggest that further anthropogenic greening will amplify HHD under future climates in the Sahel[11], any benefits from LCLUC adaptations like the GGW need to be balanced against potential harm that increased HHD exposure poses[13–16]. Additional moisture may contribute to achieving the goals of the GGW[3] because Sahelian farmers are dependent on rainfed agriculture[37]. Increased precipitation may be harnessed for agriculture production, pastoralism, and agroforestry. Furthermore, elevated precipitation may also increase background greening[6–8], reducing desertification. Such greening may reduce air temperatures[38, 39]. But heat exposure risks assessments using only air temperature can underestimate humid-heat risks to health and well-being[40].

Indeed, any influx of atmospheric moisture during planting and harvesting may worsen HHD risks for the tens of millions of rural Sahelians who rely on this moisture to produce food, especially during the crop calendar. The planting season is during April and May, with the broader crop calendar extending from April–October[17], overlapping with the most rapid increase in HHD frequency and intensity. Global-scale research shows that the Sahel is already a hotspot for labor loss due to humid-heat exposure – from both reduction in hours and economic output[16]. Labor loss

due to humid-heat exposure is equivalent to 13% of Sudan's GDP, 8% of Chad's GDP and 7% of Mali's GDP[16]. While these findings do not separate out economic loss specifically among agriculture workers, 52%, 88%, and 79% of the workforce in Sudan, Chad, and Mali were employed in agriculture in 2022[41]. Furthermore, under 3°C of mean global warming, projections of labor loss due to humid heat exposure for West Africa show the agricultural sector faces the greatest future reduction in labor[42]. Thus, any further greening through the GGW may harm the people intended to benefit the most.

While we document the historical spatiotemporal intersection of HHD dynamics and LCLUC, projecting that nearly all Sahelian residents may face >60 HHD by 2050 showcases the urgent need to deploy feasible and cost-effective adaptations[43]. For example, recent research from Kenya shows that low-cost cool roofs may reduce indoor humid-heat conditions[44]. Heat early warning systems (EWS) have also been suggested as effective adaptations[45,46]. But EWS require at-risk populations to be able to access other adaptations, like air conditioning or fans. Air conditioning is the most effective adaptation[47]. But given widespread poverty, unreliable electricity, and reliance on outdoor labor, air conditioning penetration may not increase sufficiently to reduce harm from increased HHD[48]. Fans are an often-cited low-cost alternative. But fan use can amplify heat stress during hot-dry extremes[49], which highlights that adaptations should account for the biophysical differences between hazardous dry versus humid heat.

Our findings are constrained by data limitations and associated uncertainties. First, while HImax is a well-established heat stress metric, other metrics, such as wet bulb globe temperature, may better capture heat stress by including additionally relevant meteorological conditions like thermal radiation and wind speed[40]. Second, our historical analysis only spans 1983–2016 due to the availability of high-resolution HHD data, and we do not measure how future population changes will affect projected HHD exposure. However, by holding population and total SV change constant in 2016, we isolate how climate-change-driven HHD increases contribute to projected exposure. Third, while the CHC-CMIP6 data[24] is the highest spatial resolution historical and projection HHD dataset available for the Sahel, the 5km SV data[25] is coarse-grained. Thus, our analysis does not capture finer-grained LCLUC patterns that can identify, for example, how changes in HHD vary between cropland and natural vegetation.

Despite these limitations, by leveraging high-resolution 5km climate data to map the nexus of LCLUC, HHD, and demographics, we reveal where there is urgent need for appropriate adaptation to reduce harm from HHD. Our analysis furthermore supports future examination of the biophysical mechanisms that underpin these processes. Indeed, across the world, 'greening' is often championed as a cost-effective means of countering the dangerous impacts of increasing air temperatures[38,39]. But greening may be associated with increased humidity, and humid-heat risks, offsetting potential benefits of increased vegetation. This is particularly important because any additional anthropogenic greening may further amplify HHD under climate change[11]. As such, the GGW initiative should incorporate a comprehensive understanding of the physical land-atmosphere dynamics in the Sahel and how such dynamics ultimately affect poverty reduction strategies. Regardless of adaptation investments, perhaps the most effective strategy to reduce harm from HHD is rapidly reducing greenhouse gas emissions worldwide. Without such a rapid reduction, climate change will continue to accelerate HHD risks across the region regardless of LCLUC patterns.

Materials and Methods

We note that ChatGPT versions 4 and 5 were used to assist in code development, data analysis, and data interpretation. All analysis was conducted with Python version 3.12.4.

Datasets

Climate data: We use historical observations and future projections of daily maximum heat index (HImax) from the Climate Hazards Center Coupled Model Intercomparison Project Phase 6 (CHC-CMIP6) dataset produced at 0.05° (~5km) spatial resolution[24]. This is the highest spatial resolution HImax observational and projection dataset available for the Sahel. CHC-CMIP6 observational HImax relies on a highly accurate ~5 km observational monthly maximum 2m air temperature record – CHIRTSmax – that combines in-situ station data with satellite thermal infrared observations[50]. CHIRTSmax is used to adjust down-scaled ERA5 climate reanalysis data to produce 5km daily maximum 2m air temperature (Tmax), relative humidity at the hour ERA5 records Tmax (RHx), daily average saturation vapor pressure (SVPavg), and daily average vapor pressure deficit (VPDavg). Following the US National Weather Service procedure[51], Tmax and RHx are combined to produce HImax. We calculate daily average actual vapor pressure (AVPavg) by subtracting SVPavg from VPDavg.

The CHC-CMIP6 projections were produced by generating down-scaled monthly deltas from multi-model means from coarse-grained CMIP6 projections that include 152 simulations across 25 models for each variable[24]. The deltas were then used to perturb, or adjust, the CHC-CMIP6 observational data. In other words, the CHC-CMIP6 projections assess what the weather on a given day from 1983–2016 may look like under a future climate. Here we use the CHC-CMIP6 projections following SSP2-4.5 – the middle of the road scenario – for 2050.
We furthermore use 0.05° (~5km) Climate Hazards group Infrared Precipitation (CHIRPS) data to estimate historical changes in total monthly rainfall[52].

LCLUC Data: We use the Long term Global Land Change (1982–2016) data from the Global Land Analysis and Discovery (GLAD) group[25]. The GLAD dataset is produced by combining multiple remote-sensed datasets – including the Advanced Very High Resolution Radiometer (AVHRR), the Moderate Resolution Imaging Spectroradiometer, and the Landsat Enhanced Thematic Mapper Plus – to generate annual global continuous vegetation fields at 0.05° (~5km) spatial resolution. Each grid cell for each year contains the fractional coverage of SV (vegetation < 5m), tree canopy (TC, vegetation >=5m) and bare ground (BG). A non-parametric trend analysis is used to measure the total percent change in all three land cover classes during 1982–2016, with pixel values (-100 to 100) representing net percent change.

Population Data: We use gridded age-sex population distributions for 2016 produced by WorldPop at the University of Southampton (*26*). Available as global mosaics at a 1km spatial resolution[26], this data is produced in a five step process. First, sub-national data on sex and group are collected from household surveys, census data, and other micro-surveys. These data are harmonized into 5-year age cohorts at administrative levels for complete global coverage. The age-sex cohorts are then converted into proportions for each age-sex cohort (i.e. females aged 25-30 comprise 5% of the total population in this district). These proportions are then applied to each pixel of WorldPop gridded population data[53], resulting in grid-cell level demographic breakdowns, such that the total

population of the cell and the population of each age-sex cohort at the administrative level are conserved. This provides gridded population distributions at 1km (30 arc seconds) spatial resolution for each age-sex cohort. For the purposes of this analysis, we aggregate the five-year cohorts into three broader cohorts: children (0-15 years old), working-aged (16-64 years old) and elderly (65+ years old).

Sahel Boundaries: To delineate the boundaries of the Sahel, we use data from[54] that defines the Sahel using temporally varying isohyets (precipitation isolines) that estimates the maximum extent of the Sahel based on historical precipitation data from CHIRPS[52].
Elevation Data: We use the 60 arc-second (~2km) Earth TOPOgraphy global relief model[55] digital elevation model (DEM) to isolate changes in SV and HHD by elevation (Figure S2).

Spatial Alignment

The CHC-CMIP6 and GLAD data are available at the same spatial resolution (0.05° or ~5km) and coordinate reference system, which reduces spatial uncertainty in our analysis. We resample the Worldpop and DEM data to align with the CHC-CMIP6, summing the Worldpop and averaging the DEM data to coarsen the data to 5km resolution.

Historical HHDs Trend and Spatial Intersection with LCLUC

We use the CHC-CMIP6 observational HImax data to isolate all HHD between 1983–2016, which we define as a day in which HImax exceeds 40.6°C. We acknowledge that there are at least 150 metrics used to measure heat stress[56] and that strict thresholds to identify HHD versus percentiles have limitations. But absolute thresholds are commonly used in heat physiological research[40]. In this case, HImax > 40.6°C is a threshold at which sun stroke and heat cramps are likely[9, 27].
For each pixel *i* (Eq. 1), we first calculate the total number of HHD per year (e.g. HHD frequency) between 1983–2016 and then estimate a linear trend (β_i) using the Theil–Sen slope estimator, a non-parametric regression method that is robust to outliers. We assess statistical significance of monotonic trends using Kendall's tau test, with $p < 0.05$ considered statistically significant. We multiply the annual slope by 34 years to estimate the total change in HHD over the 1983–2016 study period.

$$Y_i = \alpha_i + \beta_i T + \epsilon_{i,t} \text{ (eq. 1)}$$

Once we identify the total change in HHD frequency (Figure 1A), we spatially overlap the GLAD SV data to map the spatial association between the change in HHD and the change in SV (Figure 1C-E). This includes binning the annual change in HHD by SV categories: SV decrease, SV no change, and SV increase. Kruskal-Wallis and pairwise MannWhitney U tests are then used to test statistical significant differences among and between the SV categories distributions. This approach is also used to assess the relationship between change in total HHD and total change in TC (Figure S7). Note that all pixels where the Theil–Sen slope is not significant are set to zero when binned by SV category. We repeat this process at the monthly scale by first calculating the total number of HHD occurring in each month of each year. We then estimate Theil–Sen slopes for each monthly time series and multiply the resulting slopes by 34 years to estimate the total change in monthly HHD frequency over 1983–2016 stratified by SV categories.

Finally, to compare total monthly HHD during the beginning of our study period to the end, we calculate the average number of HHD for each month during the first decade (1983–1992) and last decade (2007–2016), as well as the difference between the two time periods (Figure S3-S5).

Influence of Tmax versus Atmospheric Moisture During HHD, 1983–2016

To isolate the contributions of dry air temperature and atmospheric moisture to changes in HHD intensity, we estimate the total change in HImax, Tmax, and moisture (AVPavg and RHx) across all HHD between 1983–2016 by SV category (Figure 3). Specifically, we estimate the fitted trend in each variable during all HHD by SV change category, then calculate the total change implied by that trend. This allows us to assess how HHD intensity, air temperatures, and atmospheric moisture changed on a given HHD over 34 years across SV categories.

We first isolate all HHD for all pixels across the Sahel. Next, we measure the aggregate influence of Tmax and atmospheric moisture (RHx and AVPavg) on the change in HImax during HHD across all HHD within each SV category (Figure 3). To do this, we pool all HHD observations by each SV category across space for each day and time (e.g. all pixels with an observed HHD for a given calendar day) to estimate trends in HImax, Tmax, RHx, and AVPavg during HHD. Trends are fitted with an ordinary least squares (OLS) slope estimator and statistical significance is assessed with Newey–West HAC standard errors. For each SV category, the slopes are multiplied by the total number of HHD that occurred between 1983-2016 (Table S1) for each metric. In other words, we measure for all HHD within a given SV category, how much HImax, Tmax, RHx, and AVPavg changed on average for a given HHD in 2016 compared to 1983. This approach captures how average HHD conditions evolve within different SV, rather than at individual pixels. This can be expressed as:

$$Y_{g,n} = \alpha_g + \beta_g n + \epsilon_{g,n} \text{ (eq. 2)}$$

Where $Y_{g,n}$ is the value of HImax, Tmax, RHx or AVPavg for the n-th HHD observation in SV category g and n is the index of all pooled HHD observations in that SV category between 1983-2016, $\beta_g$is the the Theil-Sen slope estimator and $\epsilon_{g,n}$ is the residual error term. Then total change over the full study period is:

$$\triangle Y_g = \beta_g \times n_g \text{ (eq. 3)}$$

To spatially identify where and how Tmax and atmospheric moisture (RHx and AVPavg) influenced the change in HImax during HHD (e.g. HHD intensity), we again isolate all HHD for all pixels across the Sahel. We then estimate the trend in HImax, Tmax, RHx, and AVPavg across all HHD for each pixel using an OLS slope estimator and statistical significance is assessed with Newey–West HAC standard errors. For each pixel, the slopes of HImax, Tmax, RHx, and AVPavg are multiplied by 34 to measure total change in each metric (Figure 4A). Finally, we bin the total change in each metric by SV category (Figure 4B). The Kruskal-Wallis test and pairwise MannWhitney U are used to test statistically significant differences among and between the SV categories distributions for each metric. Note that all pixels where Theil–Sen slope is not significant are set to zero when binned by SV category. We repeat this process to produce total change estimates binned by SV category for each metric by month (Figures S8-S11). We also use this process to estimate total changes in total rainfall by month using CHIRPS data (Figure S12).

Historical Exposure and 2050 Projections

We estimate historical total exposure to HHD by age-cohorts across SV categories by first totaling the number of HHD during 2016 across the Sahel. We then estimate the number of people exposed to HHD categories: 0 HHD, 1-30 HHD, 30-60 HHD, and >60 HHD in 2016. We bin populations exposed to these HHD by age cohorts (0-15, 16-64, and 65+ years old). To estimate total exposure, we multiply the average number of HHD by the number of people exposed (person-days) at the pixel-level and then sum the total. We repeat the same process using the CHC-CMIP6 SSP2-4.5 2050 projection for 2016 holding population and total SV change categories constant for 2016.

References

1. E. Eboreime, O. Anjorin, C. Obi-Jeff, T. M. Ojo, A. Hertelendy, From drought to displacement: Assessing the impacts of climate change on conflict and forced migration in West Africa's Sahel Region. J. Clim. Change Health **23**, 100448 (2025).

2. W. Anderson, C. Taylor, S. McDermid, E. Ilboudo-Nébié, R. Seager, W. Schlenker, F. Cottier, A. de Sherbinin, D. Mendeloff, K. Markey, Violent conflict exacerbated drought-related food insecurity between 2009 and 2019 in sub-Saharan Africa. Nat. Food, 1–13 (2021).

3. The Great Green Wall Implementation Status and WAy Ahead to 2030. https://www.unccd.int/sites/default/files/2024-08/1551_GGW_Report_ENG_Final_040920.pdf.

4. A. L. Zhu, A. Ndiaye, R. Dahm, M. Mauclaire, I. Boas, Africa's Great Green Mirage? Assessing the disconnect between global finance and local implementation in Africa's Great Green Wall. Land Use Policy **157**, 107670 (2025).

5. Get Africa's Great Green Wall back on track. Nature **587**, 8–8 (2020).

6. T. Hickler, L. Eklundh, J. W. Seaquist, B. Smith, J. Ardö, L. Olsson, M. T. Sykes, M. Sjöström, Precipitation controls Sahel greening trend. Geophys. Res. Lett. **32** (2005).

7. S. Piao, X. Wang, T. Park, C. Chen, X. Lian, Y. He, J. W. Bjerke, A. Chen, P. Ciais, H. Tømmervik, R. R. Nemani, R. B. Myneni, Characteristics, drivers and feedbacks of global greening. Nat. Rev. Earth Environ. **1**, 14–27 (2020).

8. Y. Zeng, L. Jia, M. Menenti, M. Jiang, B. A. Barnieh, A. Bennour, Y. Lv, Changes in vegetation greenness related to climatic and non-climatic factors in the Sudano-Sahelian region. Reg. Environ. Change **23**, 92 (2023).

9. M. B. Sylla, A. Faye, F. Giorgi, A. Diedhiou, H. Kunstmann, Projected Heat Stress Under 1.5 °C and 2 °C Global Warming Scenarios Creates Unprecedented Discomfort for Humans in West Africa. Earths Future **6**, 1029–1044 (2018).

10. C. E. Birch, L. S. Jackson, D. L. Finney, J. M. Marsham, R. A. Stratton, S. Tucker, S. Chapman, C. A. Senior, R. J. Keane, F. Guichard, E. J. Kendon, Future Changes in African Heatwaves and Their Drivers at the Convective Scale. doi: 10.1175/JCLI-D-21-0790.1 (2022).

11. R. Ingrosso, F. S. R. Pausata, Contrasting consequences of the Great Green Wall: Easing aridity while increasing heat extremes. One Earth **7**, 455–472 (2024).

12. A. Dajuma, M. B. Sylla, M. Tall, M. Almazroui, E. Afiesimama, A. Dosio, W. Moufouma-Okia, A. Diedhiou, F. Giorgi, Projected Intensification and Expansion of Heat Stress and Related Population Exposure Over Africa Under Future Climates. Earths Future **12**, e2024EF004646 (2024).

13. C. Brimicombe, K. Wieser, T. Monthaler, D. Jackson, J. D. Bont, M. F. Chersich, I. M. Otto, Effects of ambient heat exposure on risk of all-cause mortality in children younger than 5 years in Africa: a pooled time-series analysis. Lancet Planet. Health **8**, e640–e646 (2024).

14. B. Asamoah, T. Kjellstrom, P.-O. Östergren, Is ambient heat exposure levels associated with miscarriage or stillbirths in hot regions? A cross-sectional study using survey data from the Ghana Maternal Health Survey 2007. Int. J. Biometeorol. **62**, 319–330 (2018).

15. C. Kroeger, Heat is associated with short-term increases in household food insecurity in 150 countries and this is mediated by income. Nat. Hum. Behav. **7**, 1777–1786 (2023).

16. L. A. Parsons, Y. J. Masuda, T. Kroeger, D. Shindell, N. H. Wolff, J. T. Spector, Global labor loss due to humid heat exposure underestimated for outdoor workers. Environ. Res. Lett. **17**, 014050 (2022).

17. V. O. Kongo, N. A. Arreyndip, The 2023 drought in West Africa and associated vulnerability to food insecurity. Sci. Rep. **15**, 34959 (2025).

18. B. Oueslati, B. Pohl, V. Moron, S. Rome, S. Janicot, Characterization of Heat Waves in the Sahel and Associated Physical Mechanisms. doi: 10.1175/JCLI-D-16-0432.1 (2017).

19. K. L. Findell, A. Berg, P. Gentine, J. P. Krasting, B. R. Lintner, S. Malyshev, J. A. Santanello, E. Shevliakova, The impact of anthropogenic land use and land cover change on regional climate extremes. Nat. Commun. **8**, 989 (2017).

20. C. Tuholske, K. Caylor, C. Funk, A. Verdin, S. Sweeney, K. Grace, P. Peterson, T. Evans, Global urban population exposure to extreme heat. Proc. Natl. Acad. Sci. **118** (2021).

21. Projections of Human Exposure to Dangerous Heat in African Cities Under Multiple Socioeconomic and Climate Scenarios - Rohat - 2019 - Earth's Future - Wiley Online Library. https://agupubs.onlinelibrary.wiley.com/doi/full/10.1029/2018EF001020.

22. E. D. Coffel, R. M. Horton, A. de Sherbinin, Temperature and humidity based projections of a rapid rise in global heat stress exposure during the 21st century. Environ. Res. Lett. **13**, 014001 (2017).

23. A. Mirzabaev, M. Sacande, F. Motlagh, A. Shyrokaya, A. Martucci, Economic efficiency and targeting of the African Great Green Wall. Nat. Sustain. **5**, 17–25 (2022).

24. E. Williams, C. Funk, P. Peterson, C. Tuholske, High resolution climate change observations and projections for the evaluation of heat-related extremes. Sci. Data **11**, 261 (2024).

25. X.-P. Song, M. C. Hansen, S. V. Stehman, P. V. Potapov, A. Tyukavina, E. F. Vermote, J. R. Townshend, Global land change from 1982 to 2016. Nature **560**, 639–643 (2018).

26. WorldPop :: Age and sex structures. https://hub.worldpop.org/project/categories?id=8.

27. About NWS Forecast Parameters, Weather Types and Hazards. https://tidesandcurrents.noaa.gov/ofs/nws_forecastinfo.html?utm_source=chatgpt.com.

28. P. I. Palmer, C. M. Wainwright, B. Dong, R. I. Maidment, K. G. Wheeler, N. Gedney, J. E. Hickman, N. Madani, S. S. Folwell, G. Abdo, R. P. Allan, E. C. L. Black, L. Feng, M. Gudoshava, K. Haines, C. Huntingford, M. Kilavi, M. F. Lunt, A. Shaaban, A. G. Turner, Drivers and impacts of Eastern African rainfall variability. Nat. Rev. Earth Environ. **4**, 254–270 (2023).

29. Trisos, C.H., I.O. Adelekan, E. Totin, A. Ayanlade, J. Efitre, A. Gemeda, K. Kalaba, C. Lennard, C. Masao, Y. Mgaya, G. Ngaruiya, D. Olago, N.P. Simpson, and S. Zakieldeen, Chapter 9: Africa. https://www.ipcc.ch/report/ar6/wg2/chapter/chapter-9/.

30. M. Biasutti, Rainfall trends in the African Sahel: Characteristics, processes, and causes. WIREs Clim. Change **10**, e591 (2019).

31. S. E. Nicholson, A. H. Fink, C. Funk, Assessing recovery and change in West Africa's rainfall regime from a 161-year record. doi: 10.1002/joc.5530.

32. D. Spät, M. Biasutti, A. Voigt, Extreme Sahelian Rainfall Continues to Rise Despite Stable Storm Frequency. doi: 10.1029/2025GL115942.

33. G. Chagnaud, C. M. Taylor, L. S. Jackson, C. E. Birch, J. H. Marsham, C. Klein, Wet-Bulb Temperature Extremes Locally Amplified by Wet Soils. Geophys. Res. Lett. **52**, e2024GL112467 (2025).

34. Q. Kong, M. Huber, Regimes of Soil Moisture–Wet-Bulb Temperature Coupling with Relevance to Moist Heat Stress. doi: 10.1175/JCLI-D-23-0132.1 (2023).

35. N. Y. Krakauer, B. I. Cook, M. J. Puma, Effect of irrigation on humid heat extremes. Environ. Res. Lett. **15** (2020).

36. C. Raymond, T. Matthews, C. Tuholske, Evening humid-heat maxima near the southern Persian/Arabian Gulf. Commun. Earth Environ. **5**, 591 (2024).

37. UNEP, Ed., Livelihood Security: Climate Change, Migration and Conflict in the Sahel (IUNEP, Geneva, 2011).

38. D. Ellison, C. E. Morris, B. Locatelli, D. Sheil, J. Cohen, D. Murdiyarso, V. Gutierrez, M. van Noordwijk, I. F. Creed, J. Pokorny, D. Gaveau, D. V. Spracklen, A. B. Tobella, U. Ilstedt, A. J. Teuling, S. G. Gebrehiwot, D. C. Sands, B. Muys, B. Verbist, E. Springgay, Y. Sugandi, C. A. Sullivan, Trees, forests and water: Cool insights for a hot world. Glob. Environ. Change **43**, 51–61 (2017).

39. Y. Li, J.-C. Svenning, W. Zhou, K. Zhu, J. F. Abrams, T. M. Lenton, W. J. Ripple, Z. Yu, S. N. Teng, R. R. Dunn, C. Xu, Green spaces provide substantial but unequal urban cooling globally. Nat. Commun. **15**, 7108 (2024).

40. J. W. Baldwin, T. Benmarhnia, K. L. Ebi, O. Jay, N. J. Lutsko, J. K. Vanos, Humidity's Role in Heat-Related Health Outcomes: A Heated Debate. Environ. Health Perspect. **131**, 055001 (2023).

41. FAOSTAT. https://www.fao.org/faostat/en/#data/OEA.

42. W. Saeed, I. Haqiqi, Q. Kong, M. Huber, J. R. Buzan, S. Chonabayashi, K. Motohashi, T. W. Hertel, The Poverty Impacts of Labor Heat Stress in West Africa Under a Warming Climate. Earths Future **10**, e2022EF002777 (2022).

595 43. V. Muccione, R. Biesbroek, S. Harper, M. Haasnoot, Towards a more integrated research framework
596 for heat-related health risks and adaptation. Lancet Planet. Health **8**, e61–e67 (2024).

597 44. B. Abong'o, D. Kwaro, T. Bange, V. Moshi, J. Simwero, J. Otima, S. Mendt, E. Ochomo, M. A.
598 Maggioni, Housing modifications for heat adaptation, thermal comfort and malaria vector control in rural
599 African settlements. Nat. Med. **32**, 518–526 (2026).

600 45. Preventing heat-related deaths: The urgent need for a global early warning system for heat | PLOS
601 Climate. https://journals.plos.org/climate/article?id=10.1371/journal.pclm.0000437.

602 46. W. M. Thiaw, E. Bekele, S. N. Diouf, D. G. Dewitt, O. Ndiaye, M. K. N. Ndiaye, P. N. Ndiaye, N.
603 Diene, M. Diouf, A. Diaw, S. Diop, F. Badj, A. Diouf, Toward Experimental Heat–Health Early Warning
604 in Africa. doi: 10.1175/BAMS-D-20-0140.1 (2022).

605 47. A. Bouchama, M. Dehbi, G. Mohamed, F. Matthies, M. Shoukri, B. Menne, Prognostic Factors in
606 Heat Wave–Related Deaths: A Meta-analysis. Arch. Intern. Med. **167**, 2170–2176 (2007).

607 48. L. Davis, P. Gertler, S. Jarvis, C. Wolfram, Air conditioning and global inequality. Glob. Environ.
608 Change **69**, 102299 (2021).

609 49. G. K. Chaseling, N. T. Vargas, L. Hospers, H. Barry, A. Harwood, C. Graham, A.-A. Bartlett, A.
610 Debray, G. Lynch, A. Capon, C. G. Crandall, M. F. Singh, Y. Mavros, P. Bi, A. Nigam, M. Chabot-
611 Blanchet, D. Gagnon, O. Jay, Thermal and Perceptual Responses of Older Adults With Fan Use in Heat
612 Extremes: A Secondary Analysis of a Randomized Clinical Trial. JAMA Netw. Open **8**, e2523810
613 (2025).

614 50. A High-Resolution 1983–2016 Tmax Climate Data Record Based on Infrared Temperatures and
615 Stations by the Climate Hazard Center in: Journal of Climate Volume 32 Issue 17 (2019).
616 https://journals.ametsoc.org/view/journals/clim/32/17/jcli-d-18-0698.1.xml.

617 51. Heat Index Equation. https://www.wpc.ncep.noaa.gov/html/heatindex_equation.shtml.

618 52. C. Funk, P. Peterson, M. Landsfeld, D. Pedreros, J. Verdin, S. Shukla, G. Husak, J. Rowland, L.
619 Harrison, A. Hoell, J. Michaelsen, The climate hazards infrared precipitation with stations—a new
620 environmental record for monitoring extremes. Sci. Data **2**, 150066 (2015).

621 53. F. R. Stevens, A. E. Gaughan, C. Linard, A. J. Tatem, Disaggregating Census Data for Population
622 Mapping Using Random Forests with Remotely-Sensed and Ancillary Data. PLOS ONE **10**, e0107042
623 (2015).

624 54. A. Pase, F. Gianoli, L. D. Felice, M. Bertoncin, M. Cherlet, A. K. García, Il respiro del Sahel.
625 Rappresentazioni di uno spazio in movimento. Riv. Geogr. Ital. - Open Access, doi: 10.3280/rgioa1-
626 2022oa13366 (2022).

627 55. ETOPO Global Relief Model, National Centers for Environmental Information (NCEI) (2020).
628 https://www.ncei.noaa.gov/products/etopo-global-relief-model.

629 56. L. G. Ioannou, K. Mantzios, L. Tsoutsoubi, S. R. Notley, P. C. Dinas, M. Brearley, Y. Epstein, G.
630 Havenith, M. N. Sawka, P. Bröde, I. B. Mekjavic, G. P. Kenny, T. E. Bernard, L. Nybo, A. D. Flouris,
631 Indicators to assess physiological heat strain – Part 1: Systematic review. Temperature **9**, 227–262 (2022).

632

Acknowledgments:

Computational efforts were performed on the Tempest High Performance Computing System, operated and supported by University Information Technology Research Cyberinfrastructure at Montana State University.

Funding:
AZ, CT, and NB were supported by the NASA Land-Cover and Land-Use Change program (grant number 80NSSC22K0470).
AZ and CT were supported by the Minerva Research Initiative (grant number FA9550-23-1-0684).
AZ received additional support from the Geospatial Core Facility at Montana State University.
CF was supported by the Famine Early Warning Systems Network via the U.S. Geological Survey (G24AC00087) and the Enhancing Meteorological Networks Partnership.

Author contributions:

Conceptualization: CT, CI, RMH
Methodology: CT, CI, EW, RMH, CF, NB, AZ, CK
Investigation: CT
Formal Analysis: CT
Visualization: CT
Funding acquisition: CT, NB, KA, CF
Project administration: CT
Writing – original draft: CT, CI, EW, RMH, CF, NB,
Writing – review & editing: SS, KA, EY, CK, AZ,

Competing interests: Authors declare that they have no competing interests.

Data, code, and materials availability: The code produced for this analysis is publicly available at [will provide GitHub repository upon publication]. The CHC-CMIP6 and CHIRPS data are available from the University of California, Santa Barbara: https://doi.org/10.21424/R47H0M. The Long-term Global Land Change (GLAD) data is available from the University of Maryland: https://glad.umd.edu/dataset/long-term-global-land-change. WorldPop age-sex structures data is available from WorldPop: https://hub.worldpop.org/project/categories?id=8. Earth TOPOgraphy global relief model digital elevation mode is available at https://www.ncei.noaa.gov/products/etopo-global-relief-model.

Supplementary Information

Figs. S1 to S12

Table S1

Supplementary Files

This is a list of supplementary files associated with this preprint. Click to download.

- TuholskeetalnatsustSMv1.docx